Modeling Self-Heating in High-Power Single-Mode Phase-Coupled Linear VCSEL Arrays

Modeling Self-Heating in High-Power Single-Mode Phase-Coupled Linear VCSEL Arrays

V. Torrelli, M. C. G. Alasio, *Member, IEEE*, M. D'Alessandro, *Member, IEEE*, A. Gullino, L. Miri, J. Lindner, S. Gronenborn, M. Goano, *Senior Member, IEEE*, and P. Debernardi

***Abstract*—We investigate the robustness of single-mode (SM) emission in high-power, large-area rectangular vertical-cavity surface-emitting lasers (VCSELs), emphasizing the impact of self-heating effects. Compared to circular geometries, large-area rectangular VCSELs provide improved heat dissipation thanks to their high geometrical aspect ratio, and higher SM output power by means of their patterned reflectivity obtainable by an array of grating reliefs. Self-heating alters the refractive index of the device. We demonstrate, experimentally and numerically, how the related thermal lensing affects the transverse modes. By misaligning the antinodes of the promoted lasing mode and the surface reliefs, self-heating degrades SM operation if not properly accounted for in the relief position design. Combining thermal and optical models, we propose numerically optimized grating relief geometries ensuring robust SM emission across varying operating temperatures.**

***Index Terms*—VCSEL, single-mode (SM) emission, thermal lensing, self-heating, optical modes, grating relief, high-power VCSEL, modeling.**

I. Introduction

VCSELS revolutionized optical communications and sensing with their high modulation bandwidth, beam quality, and capability of single-mode (SM) emission, essential for efficient fiber coupling and short-range high-speed datacenter communications [1], [2]. Initially, the strong demand for VCSELs in datacom applications led research towards small circular oxide-aperture designs [3], [4]. While inherently single-mode, these compact devices suffer from substantial limitations in maximum optical power due to their small active areas and associated thermal constraints.

High-power VCSELs relying on larger active areas have become relevant for a variety of applications such as plastic welding, industrial heating processes, and skin treatment [5], [6]. More recently, they are being applied to three-dimensional (3D) sensing applications such as LiDARs, where higher optical powers are required for extended-range detection [7], [8], [9], [10]. In atomic-based devices such as atomic clocks, quantum gyroscopes and atomic magnetometers, the optical pumping demands for high-power with the additional requirement of SM and single-polarization emission to accurately excite specific atomic energy transitions [11], [12], [13], [14], [15], [16].

For all VCSELs, the behavior at high injection currents is challenging, as self-heating becomes substantial and eventually leads to their turn-off. The main thermal sources in VCSELs are Joule heating, free-carrier absorption [17], carrier non-radiative recombination [18], [19] and carrier thermalization in the quantum wells (QWs) [20], [21]. These induce a non-uniform temperature distribution across the VCSEL, peaked at the QW section and transversely depending on the shape of the active area, modifying the refractive index [22], [23]. This causes the thermal lensing phenomenon, manifesting as a shrinkage of all the modes towards the device central axis, with a corresponding increase of far-field (FF) divergence.

Here, we analyze the impact of self-heating on the preservation of SM emission in high-power VCSEL designs, building on the work presented in [24], where thermal lensing was neglected.

II. Motivation From Experimental Evidence

Large-area VCSELs have emerged as promising candidates to achieve higher output power for atomic devices [25], [26], [27]. More efficient thermal dissipation was achieved for elongated active areas, specifically using large-area rectangular oxide apertures [5], [6]. Consequently, the roll-over point in the light-current (LI) characteristic is delayed towards higher bias currents compared to circular or square VCSELs with the same active area.

Achieving high-power SM operation in large-area rectangular VCSELs poses significant challenges. Indeed, increasing the aperture size to enhance the output power leads to uncontrolled multimode emission, negatively impacting beam quality and limiting practical usability [5], [6].

Received 9 June 2025; accepted 4 July 2025. Date of publication 10 July 2025; date of current version 22 July 2025. This work was supported in part by European Union under two initiatives of the Italian National Recovery and Resilience Plan (NRRP) of NextGenerationEU through the partnership on Telecommunications of the Future under Grant PE00000001– program "RESTART", in part by the National Centre for HPC, Big Data and Quantum Computing, under Grant CN00000013 – CUP E13C22000990001, and in part by the Qyro Project through the German Federal Ministry of Education and Research under Grant 13N16314. *(Corresponding author: M. C. G. Alasio.)*

V. Torrelli, M. D'Alessandro, and M. Goano are with the Department of Electronics and Telecommunications (DET), Politecnico di Torino, 10129 Turin, Italy, and also with the Istituto di Elettronica e di Ingegneria dell'Informazione e delle Telecomunicazioni (IEIIT) del Consiglio Nazionale delle Ricerche (CNR), Politecnico di Torino, 10129 Turin, Italy.

M. C. G. Alasio and L. Miri are with the Department of Electronics and Telecommunications (DET), Politecnico di Torino, 10129 Turin, Italy (e-mail: matteo.alasio@polito.it).

A. Gullino and P. Debernardi are with the Istituto di Elettronica e di Ingegneria dell'Informazione e delle Telecomunicazioni (IEIIT) del Consiglio Nazionale delle Ricerche (CNR), Politecnico di Torino, 10129 Turin, Italy.

J. Lindner and S. Gronenborn are with TRUMPF Photonic Components GmbH, 52074 Aachen, Germany.

Digital Object Identifier 10.1109/JPHOT.2025.3587464

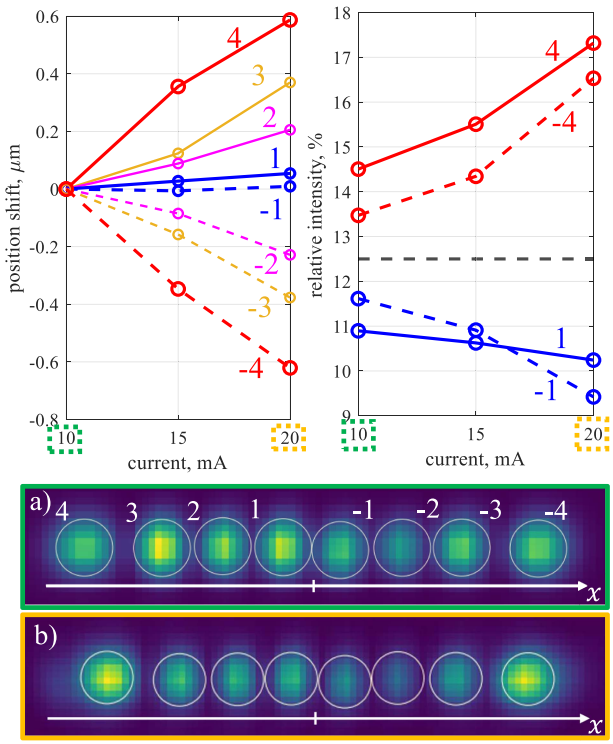

Fig. 1. Experimental evidence of peak position shifts (top left) and relative intensities (top right) for the innermost and outermost peaks of a VCSEL selecting the (7,0)-mode. Relative intensities are normalized to the total intensity and the dashed black line represents the ideal case where power is equally distributed among all peaks. The data represent averages over multiple devices. At the bottom, NF profiles of a specific device are shown for $I = 10$ mA (a) and $I = 20$ mA (b). White circles represent the regions associated to the various peaks, automatically detected by the NF camera software. Peak position shifts are calculated relative to their positions at $I = 10$ mA, with the sign convention defined according to the reference frame used in the NF plots.

The optical modes of these devices can be identified by the number of optical nodes along the wide and narrow side of the rectangle, i.e., n_x and n_y, respectively. In this way, each mode is identified by the pair (n_x, n_y). Targeting the emission of a specific (n_x, n_y) mode, in [24] we proposed to etch grating relief arrays in correspondence of the intensity peaks of the targeted mode into the VCSEL outcoupling facet, showing the potential of obtaining SM emission. This idea was applied to VCSELs emitting at 795 nm in [28], designed for quantum gyroscopes.

As mentioned in Section I, our goal is to analyze the behavior of rectangular VCSELs featuring a grating relief array with increasing self-heating. In fact, self-heating leads to losing SM emission, as the temperature-dependent refractive index significantly alters the mode shape and intensity distribution, causing misalignment between the targeted optical mode and the patterned grating reliefs. Such misalignment is the primary cause of SM emission degradation at high injection currents. An experimental evidence of field deformation with temperature is illustrated in Fig. 1, where the near-field (NF) of a VCSEL designed to favor the (7,0) mode is displayed at varying currents. Measurements are performed by means of the Instrument Systems VTC 4000 near-field camera. The considered AlGaAs VCSELs are presented in [28], featuring a standard epistructure with $\lambda/4$-thick layers for the top and bottom AlGaAs distributed Bragg reflectors (DBRs) and a λ -cavity. The topmost layer of the top DBR is initially grown to be out-of-phase, however it is locally brought into phase by the etching of the grating reliefs according to the design rules presented in [24], creating a transversely patterned reflectivity profile. In this way, the selected higher-order mode, whose lobes align with the reliefs, features a lower threshold gain than all other modes, allowing for SM high-power emission. Experimental LIV curves reported in [28] show powers above 15 mW, with single-mode operation proven by spectral analysis.

The top left graph illustrates how thermal lensing causes all peak positions to shift toward the center of the active area. Peaks are numbered starting from the center, with the sign convention reflecting their position on either the left or right side of the rectangle, respectively. The top right plot reports the normalized intensity variation of the inner peaks (1) – (−1) compared to the outer ones (4) – (−4). At 10 mA there still is a good balance between peaks (4) – (−4) and (1) – (−1), which are close to the ideal case of equally strong peaks, as displayed in the NF profile of Fig 1(a). Conversely, at 20 mA the intensity of the innermost (1) – (−1) peaks weakens in favor of the outermost (4) – (−4) lobes, as highlighted by the NF in Fig. 1(b).

Using thermal and optical simulations, we interpret the experimental observations of Fig. 1 and we provide optimized design guidelines for grating relief arrays tailored to either low- or high-temperature operating regimes.

III. Thermal Model

In previous works, we extracted the temperature profile in circular VCSELs by solving the static heat equation in conjunction with carrier transport and optical simulations [29], [30], leveraging the cylindrical symmetry to reduce the computationally demanding 3D drift-diffusion (DD) model into a two-dimensional (2D) problem. However, extending this methodology for non-cylindrical problems is computationally prohibitive. To this end, we adopt the simplified approach introduced in [31]. Defining $T(\mathbf{r})$ as the internal temperature distribution of the VCSEL, $\kappa(\mathbf{r})$ as the spatially dependent thermal conductivity and $Q(\mathbf{r})$ as the heat source, the steady-state heat equation is given by:

$$\nabla \cdot (\kappa \nabla T) = -Q. \tag{1}$$

This equation can be solved implementing a finite element method (FEM), imposing a Dirichlet boundary condition at the bottom of the substrate with a null temperature value. Consequently, the computed temperature T directly represents the temperature rise relative to the thermal reservoir, set at the heat sink temperature T_{HS}, so that the absolute temperature T_{tot} is:

$$T_{\text{tot}}(\mathbf{r}) = T_{\text{HS}} + T(\mathbf{r}). \tag{2}$$

The employed conductivity values κ for different layers of AlGaAs-based VCSELs are summarized in Table I [29], [31].We approximate Q with a piecewise heat-source, validated against

TABLE I
THERMAL CONDUCTIVITY VALUES FOR DIFFERENT SECTIONS OF ALGAAS VCSELS

Layer	κ ($\mathrm{Wm^{-1}K^{-1}}$)
Substrate	46
DBRs, active region, mesa (transverse)	15
DBRs, active region, mesa (longitudinal)	12
Passivation	0.5

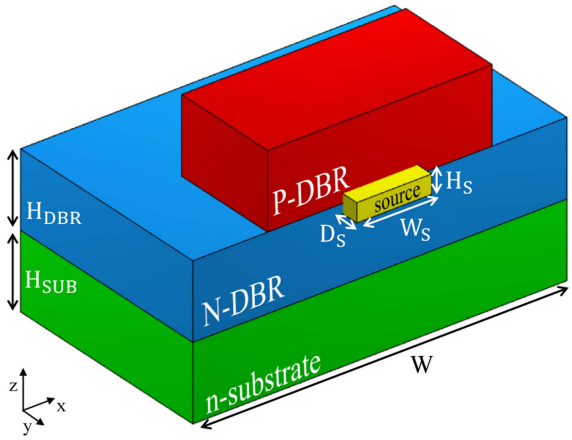

Fig. 2. Perspective view of the thermal simulation domain, indicating key geometrical parameters and highlighting the simplified heat source, placed at the QW region. The mesa is encapsulated in a passivation layer, omitted here for clarity.

our comprehensive electro-opto thermal model for circular geometries in [31]. Q can be expressed as:

$$Q(\mathbf{r}) = \begin{cases} P_{\mathrm{diss}}/V_{\mathrm{s}}, & \mathbf{r} \in V_{\mathrm{s}}, \\ 0, & \mathbf{r} \notin V_{\mathrm{s}}, \end{cases} \tag{3}$$

where V_{s} is the volume in which the source is applied and P_{diss} is the dissipated thermal power, that can be extracted from experimental LIV characteristics as:

$$P_{\mathrm{diss}} = V_{\mathrm{bias}} \cdot I_{\mathrm{bias}} - P_{\mathrm{opt}}, \tag{4}$$

with $V_{\mathrm{bias}} \cdot I_{\mathrm{bias}}$ representing the input electrical power and P_{opt} the emitted optical power. Fig. 2 reports a perspective view of the computational domain, with particular emphasis on V_{s}, identified by the yellow box and transversely defined by the oxide aperture.

IV. OPTICAL MODEL

To predict how thermal lensing affects the transverse modes of a VCSEL, we use our inhouse 3D eigenmode solver, the VCSEL ELectro Magnetic Suite (VELMS) [32]. In VELMS, the phasor of the unknown electrical field supported by the VCSEL is expanded in terms of the modes of an unbounded homogeneous reference medium with arbitrary dielectric constant $\varepsilon_{\mathrm{ref}}$. We describe the reference medium modes with cylindrical waves, whose analytical expression can be found in [33]. Each cylindrical wave is identified by a multi-label $\boldsymbol{\mu}$, which contains: type of propagation (either forward or backward), azimuthal order and angular dependency, polarization (TE or TM), and transverse wavevector. For a given structure, the number of basis functions that sufficiently describes the VCSEL modes is selected by limiting the considered azimuthal orders and by discretizing the transverse wavevector with Δk_t steps up to a maximum value, so that the whole unknown field is approximated by a finite number, N, of basis functions. The whole VCSEL can be sliced into longitudinally invariant layers and, using the coupled mode equations in matrix form [32], it is possible to obtain the transmission matrix of each layer as:

$$\mathbf{T} = e^{\mathbf{B}+\Delta k_t \mathbf{K}}, \tag{5}$$

where $\mathbf{B} \in \mathbb{C}^{N\times N}$ is a diagonal propagation matrix and $\mathbf{K} \in \mathbb{C}^{N\times N}$ is the coupling matrix.

An essential component of this methodology is the coupling matrix $\mathbf{K}$ for each layer. Defining $\mathbf{e}_{\boldsymbol{\mu}}$ and $\mathbf{e}_{\boldsymbol{\nu}}$ as the transverse components of the $\boldsymbol{\mu}$-th and $\boldsymbol{\nu}$-th basis modes, the dominant part of the $(\boldsymbol{\mu}, \boldsymbol{\nu})$-th entry of the coupling matrix, $K_{\boldsymbol{\mu\nu}}$, reads [32]:

$$K_{\boldsymbol{\mu\nu}} = -\frac{j\omega}{C_{\boldsymbol{\mu}}} \int_{\mathbb{R}^2} (\varepsilon - \varepsilon_{\mathrm{ref}})\, \mathbf{e}_{\boldsymbol{\mu}} \cdot \mathbf{e}_{\boldsymbol{\nu}}\, \mathrm{d}x\mathrm{d}y, \tag{6}$$

where ω is the optical pulsation, C_{μ} the power normalization constant and ε the dielectric constant of the considered layer. After including the thermal effects as described in Section III, the temperature dependence of the VCSEL refractive index, n, can be linearized around T_{HS} [34] as:

$$n(T) = n_{\mathrm{HS}} + \frac{\mathrm{d}n}{\mathrm{d}T} T, \tag{7}$$

where $n_{\mathrm{HS}} = n(T_{HS})$ and $\mathrm{d}n/\mathrm{d}T = 2.3 \times 10^{-4}\,(^{\circ}\mathrm{C})^{-1}$ for AlGaAs VCSELs [31], [34]. The refractive index can be converted into the dielectric constant as:

$$\varepsilon = \varepsilon_0 \left(n_{\mathrm{HS}} + \frac{\mathrm{d}n}{\mathrm{d}T} T \right)^2 \approx \varepsilon_{\mathrm{HS}} + 2\varepsilon_0 n_{\mathrm{HS}} \frac{\mathrm{d}n}{\mathrm{d}T} T, \tag{8}$$

where ε_0 is the vacuum dielectric constant, $\epsilon_{\mathrm{HS}} = \epsilon_0 n_{\mathrm{HS}}^2$ and the quadratic term in T is neglected as it represents a second order effect. In this way, (6) can be written as

$$K_{\boldsymbol{\mu\nu}} = K^{\mathrm{HS}}_{\boldsymbol{\mu\nu}} + K^{T}_{\boldsymbol{\mu\nu}}, \tag{9}$$

with

$$K^{\mathrm{HS}}_{\boldsymbol{\mu\nu}} = -\frac{j\omega}{C_{\boldsymbol{\mu}}} \int_{\mathbb{R}^2} (\varepsilon_{\mathrm{HS}} - \varepsilon_{\mathrm{ref}})\, \mathbf{e}_{\boldsymbol{\mu}} \cdot \mathbf{e}_{\boldsymbol{\nu}}\, \mathrm{d}x\mathrm{d}y, \tag{10}$$

$$K^{T}_{\boldsymbol{\mu\nu}} = -\frac{j\omega}{C_{\boldsymbol{\mu}}} \int_{\mathbb{R}^2} \left(2\varepsilon_0 n_{\mathrm{HS}} \frac{\mathrm{d}n}{\mathrm{d}T} T \right) \mathbf{e}_{\boldsymbol{\mu}} \cdot \mathbf{e}_{\boldsymbol{\nu}}\, \mathrm{d}x\mathrm{d}y. \tag{11}$$

$K^{\mathrm{HS}}_{\boldsymbol{\mu\nu}}$ describes structural transverse variations, e.g., the confinement due to the oxide layer, while $K^{T}_{\boldsymbol{\mu\nu}}$ also describes the confinement due to thermal lensing. When dealing with transverse shapes that can be analytically parametrized in polar coordinates, the angular part of the double integrals in (10)–(11) can be calculated analytically, significantly speeding up calculations. For this reason, in Section V, the self-heating temperature contour lines are approximated by ellipses.

The transmission matrix of all layers, together with the reflection at the two boundaries of the resonator, are used to set up a Barkhausen roundtrip condition. From the latter we obtain

TABLE II
GEOMETRICAL PARAMETERS OF THE STRUCTURE UNDER INVESTIGATION

Dimension	Value
W	200 μm
H_{sub}	120 μm
W_S	26 μm
D_S	6 μm
H_S	0.5 μm
H_{DBR}	5.2 μm

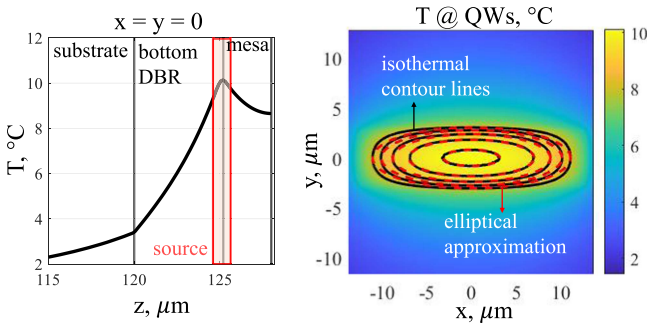

Fig. 3. Left: longitudinal self-heating temperature profile along the VCSEL symmetry axis. The different sections of the VCSEL are identified, from the substrate, to the bottom DBR and the mesa. Red lines identify the region where the uniform simplified heat source is placed, in correspondence of the QW section. Right: transverse self-heating temperature profile at the QW section, highlighting how isothermal contour lines (black lines) can be well approximated by ellipses (dashed red lines).

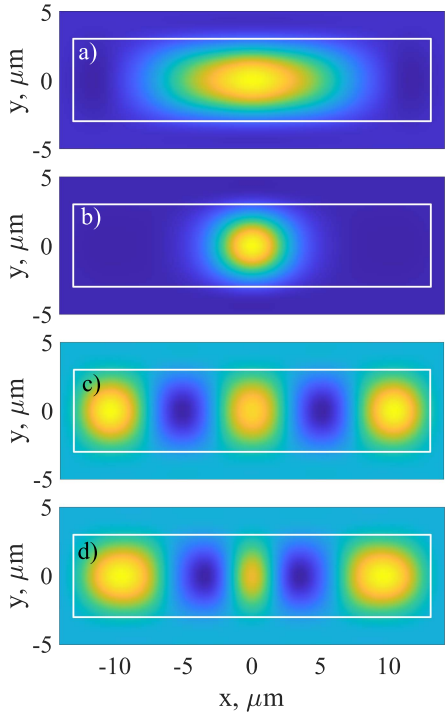

Fig. 4. Effect of self-heating on the NF profiles of the fundamental (0,0) at $P_{diss} = 0$ mW (a) and $P_{diss} = 10$ mW (b) and of the targeted mode (4,0) at $P_{diss} = 0$ mW (c) and $P_{diss} = 10$ mW (d).

the vector of the expansion coefficients, used to reconstruct the field profile (exploiting the chosen basis functions), the emission wavelength and the threshold gain for each mode supported by the VCSEL structure.

V. RESULTS AND DISCUSSION

We can now apply the methodologies described in the previous sections to the device under study for high-power SM emission, namely the 795 nm VCSEL described in [24] featuring a rectangular active area of $26 \times 6\ \mu m^2$ and a grating relief array. The values of the employed geometrical parameters, sketched in Fig. 2, are reported in Tab. II.

Using the thermal source in (3) with a case study of $P_{diss} = 5$ mW, we obtain the inner temperature profile displayed in Fig. 3, featuring a maximum temperature rise of $T_{max} = 10$ °C. The heat (1) is linear if we neglect the dependency of κ on temperature [35]. Changing P_{diss} only modifies the corresponding temperature profile by a multiplicative factor, with the peak self-heating temperature that can be calculated as $T_{max} = \eta P_{diss}$, where η is a conversion factor, obtainable as $\eta = 10\,°C/(5\,mW) = 2\,°C/mW$. Using the temperature profile reported in Fig. 3, we can compute the VCSEL refractive index exploiting (7), and run optical simulations for any given P_{diss}.

Let us start with the bare rectangular VCSEL with neither grating reliefs nor thermal lensing, that sustains the modes reported in [24], extremely close in threshold gain. Similarly to [24], we aim to select the mode (4,0) by introducing modal threshold penalties for all the other modes by designing an array of grating reliefs. We prioritize this mode as it features the most circular contour lines of the intensity profile, since the number of intensity peaks is close to the considered aspect ratio of 4.33.

To properly design the reliefs that would allow the SM emission of mode (4,0), we need to know how the modal topographies evolve with temperature. Let us investigate how the mode (4,0) and the fundamental mode (0,0), taken for reference, change with dissipated power. In Fig. 4, the corresponding NF profiles at $P_{diss} = 0$ (a)–(c) and 10 mW (b)–(d) are reported. One can notice how the effect of self-heating on the (0,0) mode causes a shrinkage towards the active area center. On the other hand, the effect on the superior mode (4,0) is more complex, showing how the various NF peaks get distorted, varying both in shape and relative intensity.

A parametric investigation of this effect is presented in Fig. 5. The selected range of dissipated powers represents a case study, and it can be scaled to any rectangular VCSEL depending on the active area, considering that the longer the rectangle, the more the innermost peaks are distorted by thermal lensing. The central peak and the two nearby peaks on the right of the (4,0) mode are labeled as peaks 0, 1, and 2, respectively (see inset in the top plot of Fig. 5). Due to the symmetry of both the oxide aperture and temperature profile, the same behavior is obtained for the peaks on the left. The plot on the top illustrates how the positions of peaks 1 and 2 shift as the dissipated power increases. The position of the peak 0 is not reported, as the problem is symmetrical and always remains in the center of the active area. As expected, the field is compressed towards the

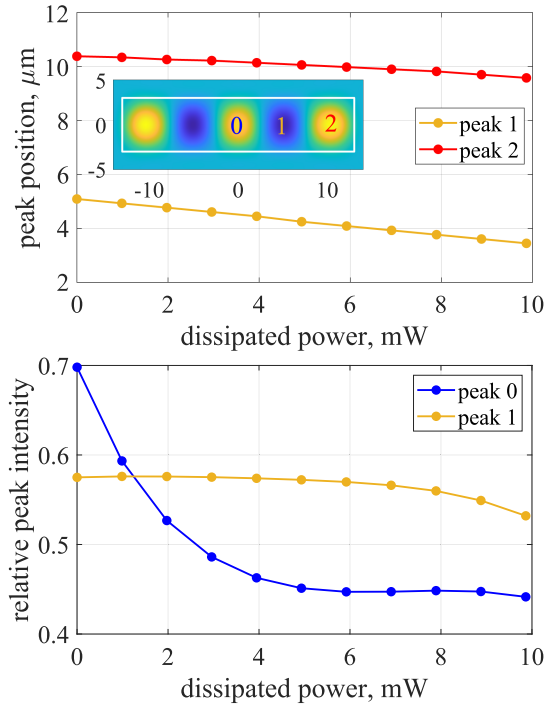

Fig. 5. Top: position of central and nearby peaks (see inset for the labels). Bottom: intensity of peaks 0 and 1, normalized to peak 2.

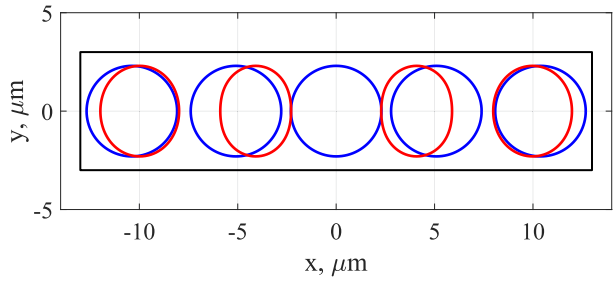

Fig. 6. Grating relief array design for low self-heating (blue), obtained through Fig. 5 using $P_{\text{diss}} = 0$ mW, and high self-heating (red), with $P_{\text{diss}} = 6$ mW.

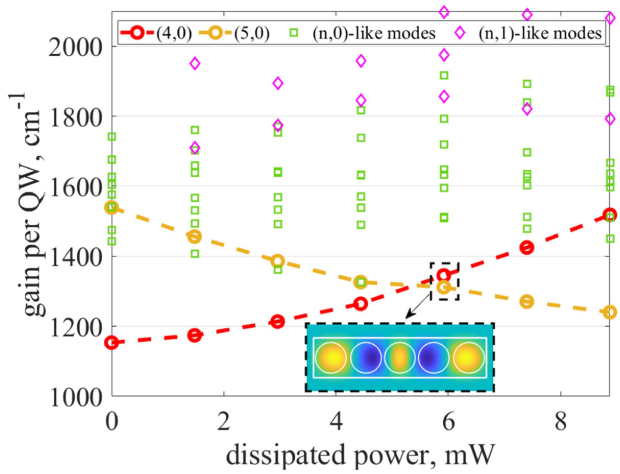

Fig. 7. Threshold gain of the transverse modes featuring the low self-heating grating relief array design described in Fig. 6. The legend highlights in red the targeted mode (4,0) and in yellow its competitor (5,0) for higher dissipated powers. Other modes featuring either zero or one node along the short direction of the active area are denoted as $(n, 0)$-like (green squares) and $(n, 1)$-like (magenta rhombuses) modes, respectively. $(n, 1)$-like modes feature higher threshold than $(n, 0)$-like modes. The inset represents the (4,0) modal field profile at the QW section with the low self-heating relief design, showing a significant misalignment between reliefs and field spots. In this plot, only the dominant polarization selected by the grating is reported.

center of the active area due to thermal lensing, resulting in a reduction of the positions of peaks 1 and 2. In contrast, the plot at the bottom shows that the intensity of the peaks 0 and 1 varies with increasing dissipated power, compared to the brightest peak 2, whose intensity is set to 1. The results qualitatively agree with the experiments in Fig. 1, indicating that our combined thermal and optical model effectively captures the behavior of higher-order modes at different bias currents. Consequently, this model can be utilized to provide design guidelines in realistic operating conditions.

The transverse shape of the grating relief array to select mode (4,0) can be optimized to have SM emission at low or high thermal lensing regime. This can be done analyzing the results in Fig. 5. By selecting a specific dissipated power, the reliefs should align with the peak positions determined from the plot at the top of Fig. 5. Similarly, the transverse area associated to each relief is influenced by the relative importance of the peaks. For instance, at high currents, the central peak 0 becomes the weakest. Furthermore, from Fig. 4, one can notice how the fundamental mode is squeezed in a very narrow portion of the active area due to thermal lensing. Therefore, for high self-heating regimes, one can etch the central relief much smaller than the lateral ones, or even not etch it at all, to avoid an unwanted selection of mode (0,0). On the other hand, a possible design for low self-heating, i.e., $P_{\text{diss}} = 0$ mW, is reported in blue in Fig. 6.

In Fig. 7, the modal threshold of all the transverse modes supported by the VCSEL with the low self-heating relief design is plotted as a function of the dissipated power. At low P_{diss}, mode (4,0) is effectively selected (see red curve). Efficient modal selection is lost above $P_{\text{diss}} = 5$ mW, where the mode (5,0) (yellow curve) features a similar threshold gain with respect to (4,0). At higher dissipated powers, (5,0) is selected instead of our targeted mode (4,0). The inset represents the targeted mode (4,0) at the QW section for $P_{\text{diss}} = 6$ mW, showing how the misalignment between the field spots and the reliefs becomes significant.

Aiming to maintain SM emission of mode (4,0) even at $P_{\text{diss}} > 5$ mW, the high self-heating design sketched with red ellipses in Fig. 6 is tested at $P_{\text{diss}} = 6$ mW. In Fig. 8, the performance of the high self-heating design (in red) in terms of modal threshold of all transverse modes is compared to the low self-heating design (in blue), showing that the former is able to retrieve a significant threshold gain difference to favor mode (4,0), also showcasing how it perfectly aligns with the new relief design. As a final remark, one can notice that the fundamental mode (0,0) threshold is extremely large for the high self-heating design. This is due to the absence of a central relief, which, if present, would have dramatically lowered the (0,0) modal

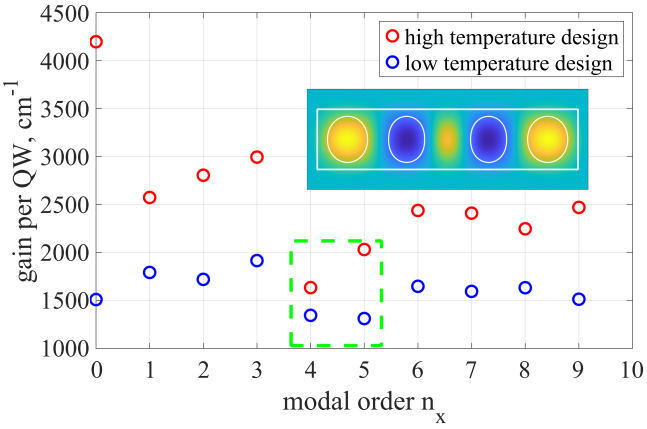

Fig. 8. Comparison between low (in blue) and high (in red) self-heating designs in terms of modal thresholds of modes (0,0), (1,0), ..., (9,0) at $P_{\text{diss}} = 6$ mW. The green dotted box identifies the region that was critical for the low self-heating design, yet it shows how a sufficient threshold difference is re-obtained for the high-self heating design. The inset shows how well the mode (4,0) aligns with the reliefs with the high self-heating design.

threshold, possibly competing with the targeted mode (4,0) and worsening the modal control.

VI. Conclusion

We analyzed the impact of self-heating on the robustness of SM emission in large-area rectangular VCSELs operating under high-power conditions. Experimental and numerical investigations showed how thermal lensing alters the spatial distribution of targeted high-order transverse modes, causing misalignment with the patterned grating relief used for modal selection.

Based on these findings, we proposed optimized grating relief arrays tailored specifically for low and high self-heating conditions. Our numerical results confirmed that separate designs are required to achieve robust SM operation across distinct thermal regimes, emphasizing the critical role of thermal management in the VCSEL design. Future work will explore more advanced strategies to dynamically maintain mode alignment, potentially extending stable high-power SM emission to a broader range of operating conditions.

Acknowledgment

The authors would also like to thank their partners Roman Koerner, Tobias Pusch and Moench Holger from TRUMPF Photonic components.

References

[1] J. A. Tatum et al., "VCSEL-based interconnects for current and future data centers," *J. Lightw. Technol.*, vol. 33, no. 4, pp. 727–732, Feb. 2015.

[2] N. N. Ledentsov et al., "High speed VCSEL technology and applications," *J. Lightw. Technol.*, vol. 40, no. 6, pp. 1749–1763, Mar. 2022.

[3] N. Ledentsov, M. Agustin, L. Chorchos, N. N. Ledentsov, and J. P. Turkiewicz, "25.78 Gbit/s data transmission over 2 km multi-mode-fibre with 850 and 910 nm single-mode VCSELs and a commercial quad small form-factor pluggable transceiver," *Electron. Lett.*, vol. 54, no. 12, pp. 774–775, 2018.

[4] A. Liu, P. Wolf, J. A. Lott, and D. Bimberg, "Vertical-cavity surface-emitting lasers for data communication and sensing," *Photon. Res.*, vol. 7, no. 2, 2019, Art. no. 121.

[5] S. Gronenborn et al., "High-power VCSELs with a rectangular aperture," *Appl. Phys. B*, vol. 105, pp. 783–792, 2011.

[6] S. Gronenborn, T. Schwarz, P. Pekarski, M. Miller, H. Mönch, and P. Loosen, "Optical modes in a rectangular VCSEL resonator with properties of both Gaussian and Fourier modes," *IEEE J. Quantum Electron.*, vol. 48, no. 8, pp. 1040–1044, Aug. 2012.

[7] J. -W. Shi, J. -I. Guo, M. Kagami, P. Suni, and O. Ziemann, "Photonic technologies for autonomous cars: Feature introduction," *Opt. Exp.*, vol. 27, no. 5, pp. 7627–7628, Mar. 2019. [Online]. Available: https://opg.optica.org/oe/abstract.cfm?URI=oe-27-5-7627

[8] I. Kim et al., "Nanophotonics for light detection and ranging technology," *Nature Nanotechnol.*, vol. 16, no. 5, pp. 508–524, 2021.

[9] M. M. Dummer, A. Ghods, G. Xu, S. Rothwell, and K. Johnson, "Single-mode multi-junction VCSELs with integrated transverse mode filter," in *Proc. SPIE*, vol. 12439, pp. 58–65, 2023.

[10] H. Moench et al., "VCSEL based sensors for distance and velocity," *Proc. SPIE*, vol. 9766, Mar. 2016, Art. no. 97660A.

[11] L. Bai et al., "Quantum-enhanced rubidium atomic magnetometer based on Faraday rotation via 795 nm stokes operator squeezed light," *J. Opt.*, vol. 23, no. 8, Aug. 2021, Art. no. 85202.

[12] M. Xun et al., "High single fundamental-mode output power from 795 nm VCSELs with a long monolithic cavity," *IEEE Electron Device Lett.*, vol. 44, no. 7, pp. 1144–1147, Jul. 2023.

[13] K. Jin et al., "Design of portable self-oscillating VCSEL-pumped cesium atomic magnetometer," *MDPI Electron.*, vol. 11, no. 22, Nov. 2022, Art. no. 3666.

[14] Y. Zhou et al., "Large-aperture single-mode 795 nm VCSEL for chip-scale nuclear magnetic resonance gyroscope with an output power of 4.1 mW at 80°C," *Opt. Exp.*, vol. 30, no. 6, pp. 8991–8999, Mar. 2022.

[15] J. Kitching, "Chip-scale atomic devices," *Appl. Phys. Rev.*, vol. 5, no. 3, 2018, Art. no. 31302.

[16] X. Jia, J. Kapraun, J. Wang, J. Qi, Y. Ji, and C. Chang-Hasnain, "Metasurface reflector enables room-temperature circularly polarized emission from VCSEL," *Optica*, vol. 10, no. 8, Aug. 2023, Art. no. 1093, doi: 10.1364/OPTICA.490176.

[17] E. Haga and H. Kimura, "Free-carrier infrared absorption in III-V semiconductors III. GaAs, InP, GaP and GaSb," *J. Phys. Soc. Jpn.*, vol. 19, no. 5, pp. 658–669, 1964.

[18] U. Strauss, W. W. Rühle, and K. Köhler, "Auger recombination in intrinsic GaAs," *Appl. Phys. Lett.*, vol. 62, no. 1, pp. 55–57, Jan. 1993.

[19] M. Takeshima, "Effect of auger recombination on laser operation in $Ga_{1-x}Al_xAs$," *J. Appl. Phys.*, vol. 58, no. 1, pp. 3846–3850, Nov. 1985.

[20] B. Deveaud, D. Morris, A. Regreny, M. R. X. Barros, P. C. Becker, and J. M. Gérard, "Quantum-mechanical versus semiclassical capture and transport properties in quantum well structures," *Opt. Quantum Electron.*, vol. 26, Art. no. S679–S689, 1994.

[21] P. W. M. Blom, J. Claes, J. E. M. Haverkort, and J. H. Wolter, "Experimental and theoretical study of the carrier capture time," *Opt. Quantum Electron.*, vol. 26, pp. S667–S677, 1994.

[22] S. Gehrsitz, F. K. Reinhart, C. Gourgon, N. Herres, A. Vonlanthen, and H. Sigg, "The refractive index of $Al_xGa_{1-x}As$ below the band gap: Accurate determination and empirical modeling," *J. Appl. Phys.*, vol. 87, no. 13, pp. 7825–7837, 2000.

[23] M. Farzaneh, R. Amatya, D. Lüerßen, K. J. Greenberg, W. E. Rockwell, and J. A. Hudgings, "Temperature profiling of VCSELs by thermoreflectance microscopy," *IEEE Photon. Technol. Lett.*, vol. 19, no. 8, pp. 601–603, Apr. 2007.

[24] V. Torrelli, A. Gullino, A. Tibaldi, F. Bertazzi, M. Goano, and P. Debernardi, "High-power emission via large-area VCSELs with single high-order mode operation," *IEEE Photon. J.*, vol. 16, no. 2, Apr. 2024, Art. no. 0600507.

[25] M. Huang, D. K. Serkland, and J. Camparo, "A narrow-linewidth three-mirror VCSEL for atomic devices," *Appl. Phys. Lett.*, vol. 121, no. 11, 2022, Art. no. 114002.

[26] M. A. Bobrov et al., "Optically pumped non-zero field magnetometric sensor for the magnetoencephalographic systems using intra-cavity contacted VCSELs with rhomboidal oxide current aperture," *J. Phys.: Conf. Ser.*, vol. 1697, no. 1, Oct. 2020, Art. no. 012175.

[27] N. A. Maleev, S. A. Blokhin, M. A. Bobrov, A. G. Kuz'menkov, M. M. Kulagina, and V. M. Ustinov, "Laser source for a compact nuclear magnetic resonance gyroscope," *Gyroscopy Navigation*, vol. 9, no. 3, pp. 177–182, 2018.

[28] J. Lindner et al., "Compact VCSEL chips for diverse applications (795nm to 850nm)," *Proc. SPIE*, vol. 13384, 2025, Art. no. 133840, doi: 10.1117/12.3043008.

[29] A. Tibaldi, F. Bertazzi, M. Goano, R. Michalzik, and P. Debernardi, "VENUS: A vertical-cavity surface-emitting laser electro-opto-thermal NUmerical simulator," *IEEE J. Sel. Topics Quantum Electron.*, vol. 25, no. 6, Nov./Dec. 2019, Art. no. 1500212.

[30] A. Gullino et al., "AlGaAs tunnel junction (TJ)-VCSELs: A NEGF-drift-diffusion approach," *IEEE Photon. J.*, vol. 16, no. 2, Apr. 2024, Art. no. 0600409.

[31] M. C. G. Alasio et al., "Modeling self-heating in high-power non-circular VCSELs," in *Proc. IEEE Photon. Conf.*, Rome, Italy, Nov. 2024, pp. 1–2.

[32] G. P. Bava, P. Debernardi, and L. Fratta, "Three-dimensional model for vectorial fields in vertical-cavity surface-emitting lasers," *Phys. Rev. A*, vol. 63, no. 2, pp. 023816-1–023816-13, 2001.

[33] A. W. Snyder and J. D. Love, *Optical Waveguide Theory*, 1st ed. New York, NY, USA: Springer, 1983.

[34] P. Debernardi, A. Tibaldi, M. Daubenschüz, R. Michalzik, M. Goano, and F. Bertazzi, "Probing thermal effects in VCSELs by experiment-driven multiphysics modeling," *IEEE J. Sel. Topics Quantum Electron.*, vol. 25, no. 6, Nov./Dec. 2019, Art. no. 1700914.

[35] S. Adachi, Ed., *Properties of Aluminium Gallium Arsenide* (EMIS Datareviews Series). London, U.K.: INSPEC, 1993.